Simple and All-Optical In-Phase and Quadrature Phase Generation Techniques

Huang, Chongjia; Albert, Chirappanath; Chan, Erwin Hoi Wing

Published in:
IEEE Photonics Journal

DOI:
10.1109/JPHOT.2022.3151642

Published: 01/04/2022

Document Version
Publisher's PDF, also known as Version of record

Simple and All-Optical In-Phase and Quadrature Phase Generation Techniques

Chongjia Huang, Chirappanath B. Albert, and Erwin H. W. Chan, *Senior Member, IEEE*

***Abstract*—New microwave photonic signal processing structures for generating in-phase and quadrature phase RF signals are presented. They are based on designing the bias angles of a dual-drive Mach Zehnder modulator (DDMZM) or a dual-parallel Mach Zehnder modulator (DPMZM) to introduce a specific phase shift to the optical carrier and using a wavelength division multiplexer to separate the lower and upper RF modulation sidebands. The optical carrier beat with the sidebands in a pair of photodetectors generate two output RF signals with a quadrature phase difference. The two proposed structures are simple, low cost and free of electrical components. The upper operating frequency of the two microwave photonic signal processors is only limited by the optical modulator bandwidth. Experimental results demonstrate the proposed microwave photonic signal processing structures have the ability to generate in-phase and quadrature phase signals with small phase and amplitude imbalance, over a wide frequency range.**

***Index Terms*—Hilbert transformer, electro-optic modulators, hybrid coupler, optical signal processing, microwave photonics.**

I. Introduction

PROCESSING radio frequency (RF) signals in an optical domain is attractive. This arises from the wideband capability of photonics, which overcomes the bandwidth limitation in conventional electronic signal processors [1], [2]. A Hilbert transformer, which produces in-phase and quadrature phase RF signals [3], is an important signal processor. It is widely used in communication systems, electronic warfare systems and instrumentation systems.

Hilbert transformers implemented using various microwave photonic techniques have been reported. Microwave photonic Hilbert transformers (MPHTs) based on a multitap transversal filter have a complex structure as they require multiple laser sources with specific wavelengths and amplitudes, and a dispersive fibre [4], [5]. Furthermore, their bandwidths are limited by the filter free spectral range. Moreover, electrical components are needed in the transversal filter based MPHTs. Using a Fourier domain optical processor (FD-OP) to implement a MPHT can simplify the structure [6], [7]. The FD-OP based MPHTs only require a single laser source, an optical modulator, a FD-OP and a pair of photodetectors. They can be designed to have a very wide bandwidth and excellent phase and amplitude imbalance performance. However, a FD-OP is bulky and costly. Recently a MPHT based on a pair of dual-polarisation dual-drive Mach Zehnder modulators (DPol-DDMZMs) operating in forward and reverse direction has been reported [8]. This MPHT can be integrated into a compact device. However, it requires six DC voltages for biasing the two DPol-DDMZMs. Note that a ring resonator [9], [10], a nonuniformly spaced delay line filter [11] and a π-phase shifted fibre Bragg grating (FBG) [12] can also be used to implement a Hilbert transformer. However, these Hilbert transformers are focused on realising the fractional Hilbert transform operation rather than generating two RF signals with a quadrature phase difference. Until now, there is no report of a simple, integrable and broadband MPHT, which is needed in electronic warfare applications [13].

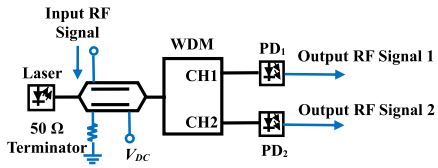

Fig. 1. Structure of the DDMZM based microwave photonic Hilbert transformer (MPHT).

This paper presents two novel all-optical MPHTs. They are based on using either a dual-drive Mach Zehnder modulator (DDMZM) or a dual-parallel Mach Zehnder modulator (DPMZM) for RF signal modulation, a wavelength division multiplexer (WDM) for separating the lower and upper sidebands, and a pair of photodetectors. The DDMZM based MPHT has a very simple structure. The DPMZM based MPHT has modulation index independent quadrature phase performance and high fundamental to second order harmonic power ratio. Experimental results are presented that demonstrate in-phase and quadrature phase RF signal generation using the two proposed MPHT structures.

II. Topologies and Operation Principle

The structure of the proposed DDMZM based MPHT is shown in Fig. 1. It consists of a laser source, a DDMZM, a WDM and two photodetectors. The DDMZM has two RF ports for RF signal modulation. One of the DDMZM RF ports is driven by the input RF signal. The other DDMZM RF port is terminated by a 50 Ω terminator. The phase difference between the two arms of the DDMZM is controlled by a DC bias voltage (V_{DC})

Manuscript received January 11, 2022; revised February 2, 2022; accepted February 11, 2022. Date of publication February 16, 2022; date of current version March 1, 2022. *(Corresponding author: Erwin H. W. Chan.)*

Chongjia Huang and Erwin H. W. Chan are with the College of Engineering, IT and Environment, Charles Darwin University, Darwin, NT 0909, Australia (e-mail: 1286660746@qq.com; erwin.chan@cdu.edu.au).

Chirappanath B. Albert is with the Department of Electrical and Electronics Engineering, Jyothi Engineering College, Thrissur 680001, India (e-mail: albertbazil@yahoo.com).

Digital Object Identifier 10.1109/JPHOT.2022.3151642

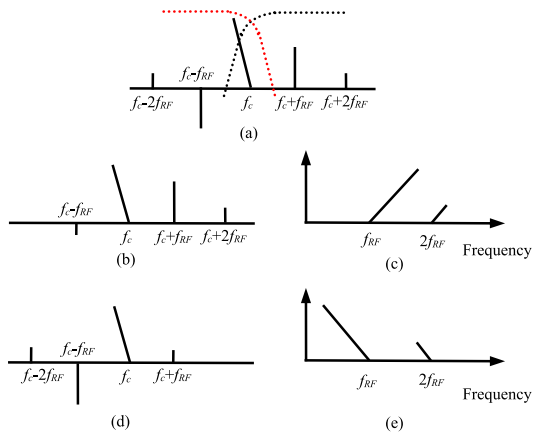

Fig. 2. (a) Optical spectrum at the DDMZM output, and WDM channel 1 (CH1) (black dotted line) and channel 2 (CH2) (red dotted line) magnitude response. Optical spectrum at WDM (b) CH1 and (d) CH2 output. (c) PD_1 and (e) PD_2 output electrical spectrum. f_c and f_{RF} are the optical carrier frequency and the input RF signal frequency respectively.

into the DDMZM DC port. The electric field at the DDMZM output is given by (1), shown at the bottom of this page, where E_{in} and ω_c are the amplitude and the angular frequency of the light wave into the DDMZM, t_{ff} is the insertion loss of the DDMZM, $J_n(x)$ is the Bessel function of nth order of the first kind, ω_{RF} is the angular frequency of the input RF signal, $\theta = \pi V_{DC}/V_{\pi,DC}$ is the DDMZM bias angle, which can be controlled by adjusting the DDMZM input DC voltage V_{DC}, $V_{\pi,DC}$ is the DDMZM DC port switching voltage, $m_{RF} = \pi V_{RF}/V_{\pi,RF}$ is the modulation index, V_{RF} is the voltage of the RF signal into the RF port of the DDMZM and $V_{\pi,RF}$ is the DDMZM RF port switching voltage.

As shown in Fig. 2(a), the DDMZM output consists of an optical carrier and two pairs of RF modulation sidebands at the frequencies of f_c, $f_c \pm f_{RF}$ and $f_c \pm 2f_{RF}$. The higher order RF modulation sidebands are neglected as they have small amplitudes. The figure also shows the magnitude responses of the two channels of the WDM connected to the DDMZM output. It can be seen from the figure that the frequency of the optical carrier is designed to be in the middle of the two WDM channels. The upper and lower RF modulation sidebands are in the passband of WDM channel 1 (CH1) and channel 2 (CH2) respectively. Fig. 2(b) and 2(d) show the two channel output optical spectrums. Since the WDM magnitude responses have a finite edge roll-off, the first order lower and upper sideband are not fully suppressed at WDM CH1 and CH2 output respectively. The electric field of the optical signals at the two WDM channel outputs are given by

$$E_{DDMZM,CH1}(t) = \frac{1}{2}E_{in}\sqrt{t_{ff}}\sqrt{L}e^{j\omega_c t} \times \begin{bmatrix} -\sqrt{\alpha(f_c - f_{RF})}J_1(m_{RF})e^{-j\omega_{RF}t} \\ +\sqrt{\alpha(f_c)}\left(J_0(m_{RF}) + e^{j\theta}\right) \\ +J_1(m_{RF})e^{j\omega_{RF}t} + J_2(m_{RF})e^{j2\omega_{RF}t} \end{bmatrix} \quad (2)$$

$$E_{DDMZM,CH2}(t) = \frac{1}{2}E_{in}\sqrt{t_{ff}}\sqrt{L}e^{j\omega_c t} \times \begin{bmatrix} J_2(m_{RF})e^{-j2\omega_{RF}t} - J_1(m_{RF})e^{-j\omega_{RF}t} \\ +\sqrt{\alpha(f_c)}\left(J_0(m_{RF}) + e^{j\theta}\right) \\ +\sqrt{\alpha(f_c + f_{RF})}J_1(m_{RF})e^{j\omega_{RF}t} \end{bmatrix} \quad (3)$$

where L is the WDM insertion loss and $\alpha(f)$ is the amount of suppression at the optical frequency f introduced by the WDM. $\alpha(f)$ equal to 1 (or 0) indicates no suppression (or full suppression) of an optical frequency component at the frequency f. For simplicity, we assume $\alpha(f_c - f_{RF}) = \alpha(f_c + f_{RF}) = \alpha(f_c \pm f_{RF})$. The two WDM channel outputs are connected to two photodetectors (PD_1 and PD_2). Beating of optical frequency components at the photodetectors generate photocurrents at the input RF signal frequency f_{RF}. The photocurrent at f_{RF} at the two photodetector outputs are given by

$$I_{DDMZM,PD1,RF}(t) = \frac{1}{2}\Re P_{in}t_{ff}L\sqrt{{A_1}^2 + {B_1}^2}\cos\left(\omega_{RF}t + \tan^{-1}\left(\frac{B_1}{A_1}\right) + \omega_{RF}\tau\right) \quad (4)$$

$$I_{DDMZM,PD2,RF}(t) = \frac{1}{2}\Re P_{in}t_{ff}L\sqrt{{A_1}^2 + {B_1}^2}\cos\left(\omega_{RF}t - \tan^{-1}\left(\frac{B_1}{A_1}\right)\right) \quad (5)$$

where $\Re$ is the photodetector responsivity, P_{in} is the power of the continuous wave light into the DDMZM,

$$A_1 = \sqrt{\alpha(f_c)}\left(1 - \sqrt{\alpha(f_c \pm f_{RF})}\right)J_1(m_{RF})\left(J_0(m_{RF}) + \cos\theta\right) + J_1(m_{RF})J_2(m_{RF}) \quad (6)$$

$$B_1 = -\sqrt{\alpha(f_c)}\left(1 + \sqrt{\alpha(f_c \pm f_{RF})}\right)J_1(m_{RF})\sin\theta \quad (7)$$

Note that a time delay τ is included in (4). It is due to a slight mismatch in the two path lengths between the WDM outputs and the photodetectors. It can be seen from (4) and (5) that the two photocurrents have the same amplitude and a phase difference of $2\tan^{-1}(B_1/A_1) + \omega_{RF}\tau$. In the case where the residual first order sidebands are largely suppressed by the WDM, the input RF signal is a small signal and the two path lengths are matched, the two photodetector output currents at the input RF signal frequency have a 90° phase difference when the DDMZM is biased at the quadrature point. This shows the proposed structure is capable to generate two RF signals with equal amplitude and quadrature phase. Note that the MPHT shown in Fig. 1 utilises a DDMZM with an input RF signal applied to one of the two arms of the DDMZM. Hence the DDMZM is not operating at the chirp-free configuration. This is required to enable the phase of the optical carrier at the DDMZM output to be controlled by the modulator bias voltage, while the sideband phase remains by

$$E_{DDMZM}(t) = \frac{1}{2}E_{in}\sqrt{t_{ff}}e^{j\omega_c t}\begin{bmatrix} J_2(m_{RF})e^{-j2\omega_{RF}t} - J_1(m_{RF})e^{-j\omega_{RF}t} + \left(J_0(m_{RF}) + e^{j\theta}\right) \\ +J_1(m_{RF})e^{j\omega_{RF}t} + J_2(m_{RF})e^{j2\omega_{RF}t} \end{bmatrix} \quad (1)$$

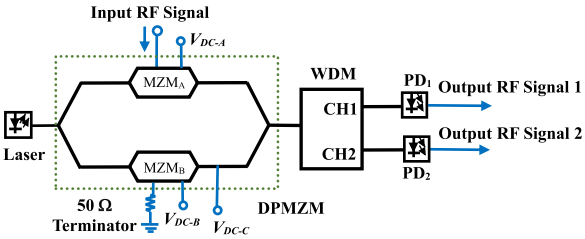

Fig. 3. Structure of the DPMZM based microwave photonic Hilbert transformer (MPHT).

unchanged, in order to obtain two RF signals with a 90° phase difference at the MPHT outputs.

Beating of the optical carrier with the second order sideband and beating of the two first order sidebands at the photodetectors generate a photocurrent at twice the input RF signal frequency $2f_{RF}$. They are given by

$$I_{DDMZM,PD1,2RF}(t) = \frac{1}{2}\Re P_{in} t_{ff} L \sqrt{{A_2}^2 + {B_2}^2} \cos\left(2\omega_{RF}t + \tan^{-1}\left(\frac{B_2}{A_2}\right) + 2\omega_{RF}\tau\right) \tag{8}$$

$$I_{DDMZM,PD2,2RF}(t) = \frac{1}{2}\Re P_{in} t_{ff} L \sqrt{{A_2}^2 + {B_2}^2} \cos\left(2\omega_{RF}t - \tan^{-1}\left(\frac{B_2}{A_2}\right)\right) \tag{9}$$

where

$$A_2 = \sqrt{\alpha(f_c)} J_2(m_{RF}) \left(J_0(m_{RF}) + \cos\theta\right) - \sqrt{\alpha(f_c \pm f_{RF})} {J^2}_1(m_{RF}) \tag{10}$$

$$B_2 = -\sqrt{\alpha(f_c)} J_2(m_{RF}) \sin\theta \tag{11}$$

It can be seen from (8) and (9) that the two output second order harmonic components have the same amplitude and a phase difference of $2\tan^{-1}(B_2/A_2)+2\omega_{RF}\tau$. The two photodetector output electrical spectrums are shown in Fig. 2(c) and 2(e).

In the second MPHT topology [Fig. 3], the DDMZM shown in Fig. 1 is replaced by a DPMZM. A DPMZM is formed by two single-drive MZMs (MZM$_A$ and MZM$_B$) connected in parallel in a main MZM [14]. Both MZM$_A$ and MZM$_B$ have an RF port and a DC port. The input RF signal is applied to MZM$_A$, which is biased at the null point for double-sideband suppressed-carrier modulation. MZM$_B$ is biased at the peak point and its RF port is terminated by a 50 Ω terminator so that only an optical carrier is present at MZM$_B$ output. The electric field at the DPMZM output is given by (12), shown at the bottom of this page, where

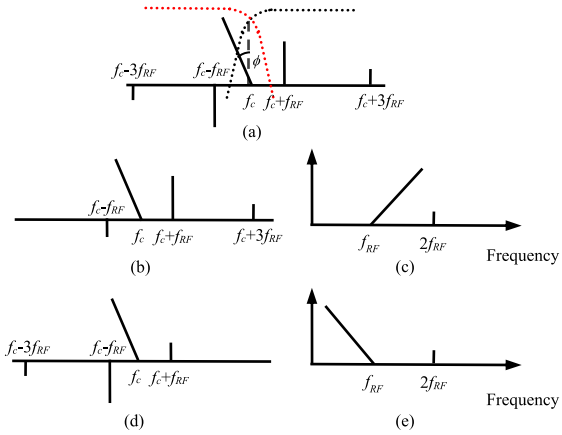

Fig. 4. (a) Optical spectrum at the DPMZM output, and WDM channel 1 (CH1) (black dotted line) and channel 2 (CH2) (red dotted line) magnitude response. Optical spectrum at WDM (b) CH1 and (d) CH2 output. (c) PD$_1$ and (e) PD$_2$ output electrical spectrum.

$\phi = \pi V_{DC\text{-}C}/V_{\pi,DC}$ is the main MZM bias angle. This shows the phase shift of the optical carrier at MZM$_B$ output can be controlled by the main MZM DC bias voltage $V_{DC\text{-}C}$. As shown in Fig. 4(a), the DPMZM output consists of an optical carrier and two pairs of RF modulation sidebands at the frequencies of f_c, $f_c \pm f_{RF}$ and $f_c \pm 3f_{RF}$. Note that, under an ideal situation, MZM$_A$ does not generate an optical carrier and the second order RF modulation sidebands. A WDM is connected to the DPMZM output. The magnitude responses of the two WDM channels are shown by the dotted lines in Fig. 4(a). As in the case of the DDMZM based MPHT, the optical carrier is in the middle of the two WDM channels. The electric field of the optical signals at the two WDM channel outputs are given by

$$E_{DPMZM,CH1}(t) = \frac{1}{2} E_{in} \sqrt{t_{ff}} \sqrt{L} e^{j\omega_c t} \times \begin{bmatrix} -\sqrt{\alpha(f_c - f_{RF})} J_1(m_{RF}) e^{-j\omega_{RF}t} + \sqrt{\alpha(f_c)} e^{j\phi} \\ +J_1(m_{RF}) e^{j\omega_{RF}t} + J_3(m_{RF}) e^{j3\omega_{RF}t} \end{bmatrix} \tag{13}$$

$$E_{DPMZM,CH2}(t) = \frac{1}{2} E_{in} \sqrt{t_{ff}} \sqrt{L} e^{j\omega_c t} \times \begin{bmatrix} -J_3(m_{RF}) e^{-j3\omega_{RF}t} - J_1(m_{RF}) e^{-j\omega_{RF}t} \\ +\sqrt{\alpha(f_c)} e^{j\phi} + \sqrt{\alpha(f_c + f_{RF})} J_1(m_{RF}) e^{j\omega_{RF}t} \end{bmatrix} \tag{14}$$

Fig. 4(b) and 4(d) show the optical spectrum at WDM CH1 and CH2 output. A residual first order RF modulation sideband is present at the two WDM outputs due to the WDM magnitude response has a finite edge roll off. The optical signals at the two WDM outputs are detected by two photodetectors (PD$_1$ and PD$_2$). Photocurrents at the input RF signal frequency f_{RF} can

$$E_{DPMZM}(t) = \frac{1}{2} E_{in} \sqrt{t_{ff}} e^{j\omega_c t} \begin{bmatrix} -J_3(m_{RF}) e^{-j3\omega_{RF}t} - J_1(m_{RF}) e^{-j\omega_{RF}t} + e^{j\phi} \\ +J_1(m_{RF}) e^{j\omega_{RF}t} + J_3(m_{RF}) e^{j3\omega_{RF}t} \end{bmatrix} \tag{12}$$

be obtained from (13) and (14), and are given by

$$I_{DPMZM,PD1,RF}(t) = \frac{1}{2}\sqrt{\alpha(f_c)}J_1(m_{RF})\Re P_{in}t_{ff}L \times \sqrt{1+\alpha(f_c \pm f_{RF}) - 2\sqrt{\alpha(f_c \pm f_{RF})}\cos(2\phi)} \times \cos\left(\omega_{RF}t + \tan^{-1}\left[\frac{(1+\sqrt{\alpha(f_c \pm f_{RF})})}{(1-\sqrt{\alpha(f_c \pm f_{RF})})}\tan\phi\right] + \omega_{RF}\tau\right) \quad (15)$$

$$I_{DPMZM,PD2,RF}(t) = \frac{1}{2}\sqrt{\alpha(f_c)}J_1(m_{RF})\Re P_{in}t_{ff}L \times \sqrt{1+\alpha(f_c \pm f_{RF}) - 2\sqrt{\alpha(f_c \pm f_{RF})}\cos(2\phi)} \times \cos\left(\omega_{RF}t - \tan^{-1}\left[\frac{(1+\sqrt{\alpha(f_c \pm f_{RF})})}{(1-\sqrt{\alpha(f_c \pm f_{RF})})}\tan\phi\right]\right) \quad (16)$$

(15) and (16) show the two photocurrents have the same amplitude. Unlike the DDMZM based MPHT, here the phases of the two RF signal photocurrents are independent to the modulation index. They are dependent on the amount of unwanted first order sideband suppression and the difference of the two path lengths between the WDM outputs and the two photodetectors. A phase difference of 90° can be obtained when the main MZM bias angle ϕ is $\pi/4$ when $\alpha(f_c \pm f_{RF}) = 0$ and $\tau = 0$. Photocurrents at the second order harmonic frequency $2f_{RF}$ are also generated at the two photodetector outputs. They are given by

$$I_{DPMZM,PD1,2RF}(t) = \frac{1}{2}\Re P_{in}t_{ff}L \times \left[J_1(m_{RF})J_3(m_{RF}) - \sqrt{\alpha(f_c \pm f_{RF})}{J_1}^2(m_{RF})\right] \times \cos(2\omega_{RF}t + 2\omega_{RF}\tau) \quad (17)$$

$$I_{DPMZM,PD2,2RF}(t) = \frac{1}{2}\Re P_{in}t_{ff}L \times \left[J_1(m_{RF})J_3(m_{RF}) - \sqrt{\alpha(f_c \pm f_{RF})}{J_1}^2(m_{RF})\right] \times \cos(2\omega_{RF}t) \quad (18)$$

(17) and (18) show the two photocurrents at the second order harmonic frequency have the same amplitude and the same phase when $\tau = 0$. More importantly, for a large unwanted first order sideband suppression, the second order harmonic photocurrent amplitude is proportional to $J_1(m_{RF})J_3(m_{RF})$, which is much smaller than $J_0(m_{RF})J_2(m_{RF})$ in the DDMZM based MPHT. Hence, only a small second order harmonic component is present at the output of the DPMZM based MPHT.

III. Simulation Results and Discussion

Phase imbalance is an important figure of merit for a Hilbert transformer [15]. It is defined as the phase difference of the two Hilbert transformer outputs deviated from 90°. Fig. 5(a) shows the simulated DDMZM based MPHT phase imbalance as a function of the amount of unwanted first order sideband suppression $\alpha(f_c \pm f_{RF})$ for different modulation indexes. It was obtained using (4)–(7). The simulation result shows the phase imbalance reduces as the amount of unwanted first order sideband suppression increases. More than 37 dB unwanted first order sideband suppression is needed to ensure the phase imbalance is below 3° for a modulation index of less than 0.6. Note from the figure that the higher the modulation index is the higher phase imbalance becomes. This is because the second order sideband amplitude increases faster than that of the first order sideband as the modulation index increases. The second and first order sidebands beat at the photodetector generates an unwanted frequency component at the input RF signal frequency, which affects the phase of the output RF signal formed by the beating of the carrier and the first order sideband. The phase imbalance can be compensated by biasing the DDMZM away from the quadrature point. Fig. 5(b) shows the required bias angle away from the quadrature point to obtain two output RF signals with a quadrature phase difference. Note that biasing the DDMZM away from the quadrature point affects the two output RF signal powers. In the case where $\alpha(f_c \pm f_{RF}) = 37$ dB and $m_{RF} = 0.6$, a bias angle of 80.5° is needed to ensure the two output RF signals have a $\pi/2$ phase difference. This causes 0.8 dB RF signal power reduction at the two Hilbert transformer outputs.

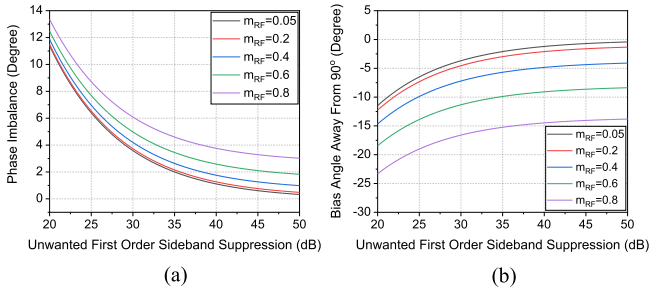

Fig. 5. (a) DDMZM based MPHT phase imbalance and (b) the required DDMZM bias angle away from 90° to obtain a quadrature phase difference at the two Hilbert transformer outputs, versus the amount of unwanted first order sideband suppression $\alpha(f_c \pm f_{RF})$ for different modulation indexes.

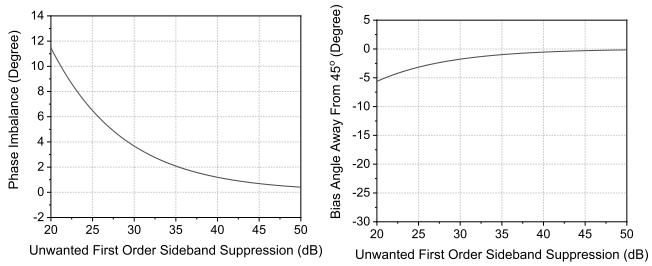

Fig. 6. (a) DPMZM based MPHT phase imbalance and (b) the required main MZM bias angle away from 45° to obtain a quadrature phase difference at the two Hilbert transformer outputs, versus the amount of unwanted first order sideband suppression $\alpha(f_c \pm f_{RF})$.

The DPMZM based MPHT phase imbalance as a function of the amount of unwanted first order sideband suppression $\alpha(f_c \pm f_{RF})$ can be obtained using (15) and (16). The simulation result given in Fig. 6(a) shows the phase imbalance is below 3° when $\alpha(f_c \pm f_{RF})$ is larger than 32 dB. Fig. 6(b) shows the required bias angle of the main MZM away from 45° in order to eliminate the phase imbalance caused by the residual first order sideband. As shown, less than 1° main MZM bias angle

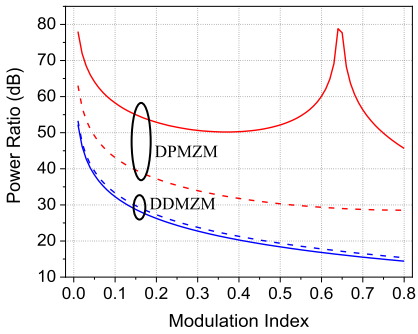

Fig. 7. Simulated fundamental to second order harmonic power ratio of the DDMZM (blue lines) and DPMZM (red lines) based MPHTs versus modulation index, for 20 dB (dashed lines) and 35 dB (solid lines) unwanted first order sideband suppression.

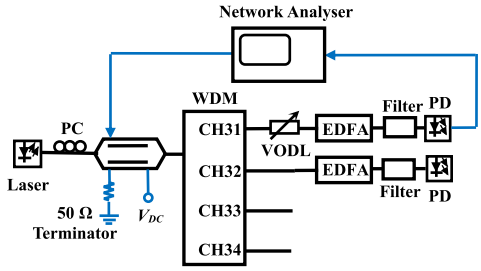

Fig. 8. Experimental setup of the DDMZM based MPHT.

away from 45° is needed to ensure the two Hilbert transformer output RF signals have a quadrature phase difference when the unwanted first order sideband suppression is over 35 dB. Fig. 7 shows the ratio of the output RF signal power to the output second order harmonic power for the two MPHTs. It can be seen from the figure that the DPMZM based MPHT has a high fundamental to second order harmonic power ratio compared to its DDMZM counterpart. In the case of the DPMZM based MPHT, the second order harmonic component increases as the amount of unwanted first order sideband suppression reduces. On the other hand, the residual first order sideband has little effects on the DDMZM based MPHT output second order harmonic component. Over 10 dB fundamental to second order harmonic power ratio improvement can still be obtained using the DPMZM structure for only 20 dB unwanted first order sideband suppression and a modulation index of above 0.2. Note from Fig. 7 that, in the case of 35 dB unwanted first order sideband suppression, the DPMZM based MPHT has a high fundamental to second order harmonic power ratio when the modulation index is around 0.65. This is because the second order harmonic is generated by the sum of the beating between the wanted first order sideband and the third order sideband, and the beating between the two first order sidebands, at the photodetector. (17) and (18) show the two generated second order harmonic components have an opposite phase, and their amplitudes are proportional to $J_1(m_{RF})J_3(m_{RF})$ and $\sqrt{\alpha}(f_c \pm f_{RF}) \cdot J_1^2(m_{RF})$. $J_1(m_{RF})J_3(m_{RF})$-$\sqrt{\alpha}(f_c \pm f_{RF}) \cdot J_1^2(m_{RF})$ is almost 0, i.e., the two second order harmonic components cancel out each other, when the amount of unwanted first order sideband suppression is 35 dB and the modulation index is around 0.65. Therefore a high fundamental to second order harmonic power ratio can be obtained under this condition.

The proposed DDMZM and DPMZM based MPHTs have the advantages of simple, compact and low-cost compared to the reported MPHTs [4]–[8]. They are both based on introducing a phase shift to the optical carrier via controlling the modulator bias voltage and separating the upper and lower sidebands via a WDM. To the best of our knowledge, using this simple technique to implement a MPHT has not been reported. The DDMZM based MPHT only requires a single DC bias voltage. A commercial bias controller, e.g., Plugtech MBC-MZM-01 MZM bias controller, which has the ability to lock the modulator at any point in the transfer function, can be incorporated into the system to obtain a long term stable performance. The DPMZM based MPHT requires three DC bias voltages. A more complex bias controller is needed to lock the modulator bias points [16]. However, compared to the DDMZM based MPHT, the DPMZM based MPHT has the advantages of modulation index independent phase imbalance performance and a small second order harmonic component. The magnitude response of a practical WDM has a limited edge roll off. Hence the unwanted first order sideband can only be largely suppressed at high frequencies. In order for the proposed MPHTs to operate at low frequencies, e.g., <20 GHz, while having small phase imbalance, the WDM can be replaced by an optical coupler followed by two sets of three cascaded thin film optical filters [17] to increase the sharpness of the overall magnitude response edges. Since the two proposed MPHTs do not involve electrical components, their upper operating frequencies are only limited by the optical modulator bandwidth, which can be made to be over 100 GHz [18].

Commercial wideband electrical hybrid couplers have a large phase imbalance. For example, Marki Microwave QH-0867 8 to 67 GHz bandwidth hybrid coupler has a maximum phase imbalance of ±18° [19]. The phase imbalance of an electrical hybrid coupler is mainly caused by small transmission line length asymmetries between the two output ports [20]. It tends to get worse at higher frequencies. Since the proposed MPHTs do not involve electrical components, they can be designed to have a small phase imbalance over a wide frequency range. They also have infinite isolation between the two output ports whereas the wideband electrical hybrid coupler only has around 15 dB isolation. The phase imbalance of the DDMZM and DPMZM based MPHTs is limited by the amount of the unwanted first order sideband suppression and the accuracy of the modulator bias setting. Plugtech MBC-MZM-01 MZM bias controller can lock the modulator bias angle to be within ±1° of the desired value. Simulation results show, for a large unwanted sideband suppression of over 40 dB and a modulator bias angle accuracy of ±1°, the phase imbalance of the DDMZM based MPHT is less than ±2°.

IV. Experimental Results

The DDMZM based MPHT was set up experimentally as shown in Fig. 8. A tunable laser (Keysight N7711A) was employed as an optical source. It generated a continuous wave light,

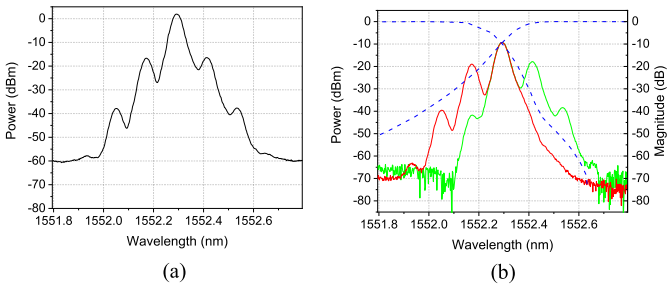

Fig. 9. (a) Measured optical spectrum at the DDMZM output. (b) Measured optical spectrums at two WDM channel outputs (solid lines). The blue dashed lines are the two WDM channel magnitude responses.

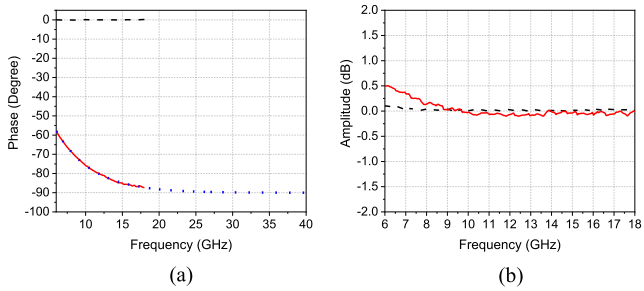

Fig. 10. (a) Phase and (b) amplitude responses of the DDMZM based MPHT measured at WDM CH31 (black dashed line) and CH32 (red solid line) output. The blue dotted line is the simulated phase difference between the two Hilbert transformer outputs.

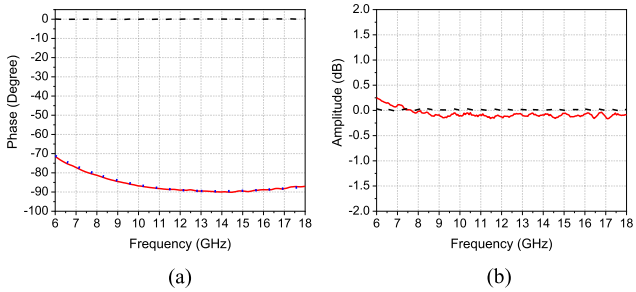

Fig. 11. (a) Phase and (b) amplitude responses of the DDMZM based MPHT measured at WDM CH31 (black dashed line) and CH32 (red solid line) output, when the two WDM channels have a slight path length difference. The blue dotted line is the simulated phase difference between the two Hilbert transformer outputs.

which was launched into a DDMZM (Fujitsu FTM7937) via a polarisation controller (PC). The DDMZM was biased close to the quadrature point. A four-channel standard WDM (AFW DWDMM-SM-D-4-1-CH31) was connected to the DDMZM output. The tunable laser wavelength was set at 1552.29 nm, which was the midpoint of two WDM channels (CH31 and CH32). The two WDM channels had a channel spacing of 0.8 nm, a 3-dB bandwidth of 0.6 nm and a channel isolation of over 25 dB. The insertion loss of the two WDM channels were measured to be around 2 dB. Fig. 9(a) shows the DDMZM output optical spectrum consists of a carrier and two pairs of upper and lower RF modulation sidebands when a 15 GHz RF signal was applied to a DDMZM RF port. Fig. 9(b) shows the normalised magnitude responses of two WDM channels around the optical carrier. It can be seen from the figure that the two WDM channel response edges are not sharp, and they have different roll offs. The two WDM channel output optical spectrums were measured and are shown in Fig. 9(b). This shows the WDM causes 10 dB suppression on the optical carrier. The lower and upper first order RF modulation sidebands at the frequency of $\pm$15 GHz away from the optical carrier have 24 dB and 30 dB suppression respectively. Note that the tunable laser has frequency stability of $\pm$0.3 GHz. Using the edge roll off of the two WDM channel magnitude responses shown in Fig. 9(b), $\pm$0.3 GHz change in the tunable laser frequency causes less than 0.5 dB change in the carrier and sideband power at the two WDM channel outputs, which has negligible effect on the MPHT phase imbalance performance. A variable optical delay line (VODL) was connected to WDM CH31 output to match the two WDM channel output path lengths. An erbium-doped fibre amplifier (EDFA) and a 0.5 nm 3-dB bandwidth optical filter were used to compensate for the modulator and WDM insertion loss and to suppress the amplified spontaneous emission noise before photodetection.

An 18 GHz bandwidth two-port vector network analyser (VNA) (Keysight E5063A) was connected to an input RF port of the DDMZM to provide a frequency sweep 6 GHz to 18 GHz RF signal to the modulator. The other port of the VNA was connected to the photodetector output to measure the output RF signal phase and amplitude responses. The phase and amplitude responses measured at one of the DDMZM based MPHT outputs were calibrated and were used as references. They are shown by the black dashed lines in Fig. 10. The phase and amplitude responses of the other Hilbert transformer output were measured and are shown by the red solid lines in Fig. 10. Due to the WDM magnitude response has a gradual edge roll off and the VNA used in the experiment has only 18 GHz bandwidth, phase imbalance of less than 3° can only be obtained in a small frequency range of 17.7 to 18 GHz. Fig. 10(a) also shows the simulated phase difference between the two Hilbert transformer outputs for different RF signal frequencies. This was obtained using (4)-(7) together with the amount of unwanted first order sideband suppression found from the edge roll off of the two measured WDM channel magnitude responses shown in Fig. 9(b). The phase difference was plotted over a wide frequency range up to 40 GHz because the upper operating frequency of the DDMZM based MPHT is only limited by the DDMZM bandwidth and most commercial wideband optical modulators have a 40 GHz bandwidth. Excellent agreement between the measured and simulated phase difference can be seen. The figure shows the phase imbalance is expected to be less than 1.5° for RF signal frequencies of above 20.8 GHz. Fig. 10(b) shows the amplitude imbalance between the two Hilbert transformer outputs is within $\pm$0.5 dB over the 6 to 18 GHz frequency range.

It was found that the phase imbalance can be reduced at low frequencies by introducing a slight path length difference between the two WDM channels via adjusting the VODL. Fig. 11 shows the measured phase and amplitude responses at the two Hilbert transformer outputs when the two WDM channels have

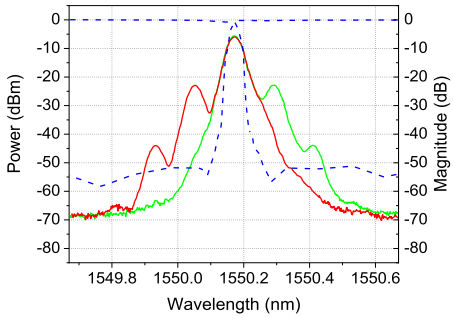

Fig. 12. Measured optical spectrums after the TOBPF when the filter centre wavelength is adjusted to filter out the lower (green line) and upper (red line) sidebands. The blue dashed lines are the corresponding TOBPF magnitude responses.

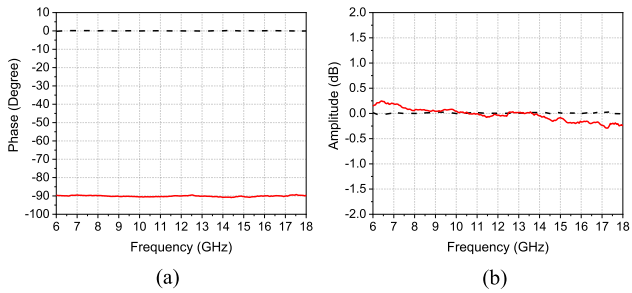

Fig. 13. (a) Phase and (b) amplitude responses of the DDMZM based MPHT measured at WDM CH31 (black dashed line) and CH32 (red solid line) output, when the TOBPF is used to filter out the unwanted sidebands.

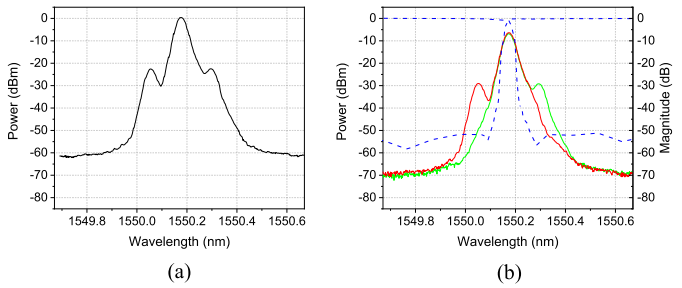

Fig. 14. (a) Measured optical spectrum at the DPMZM output. (b) Measured optical spectrums after the TOBPF when the filter centre wavelength is adjusted to filter out the lower (green line) and upper (red line) sidebands. The blue dashed lines are the corresponding TOBPF magnitude responses.

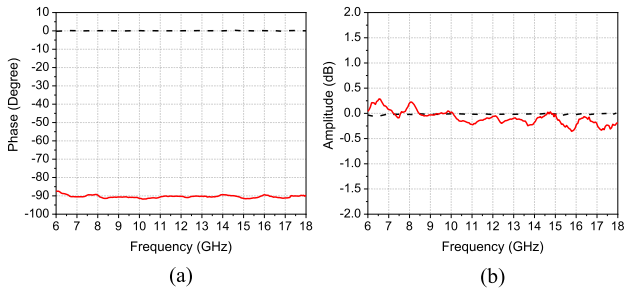

Fig. 15. (a) Phase and (b) amplitude responses of the DPMZM based MPHT measured at WDM CH31 (black dashed line) and CH32 (red solid line) output, when the TOBPF is used to filter out the unwanted sidebands.

a slight path length difference. In this case, less than 3° phase imbalance can be obtained over a frequency range of 10.4 GHz to 18 GHz. The amplitude imbalance is within ±0.3 dB over the entire 6 to 18 GHz frequency range. Fig. 11(a) also shows the simulated phase difference between the two Hilbert transformer outputs for the two WDM channels having a 0.92 mm path length difference. Again, excellent agreement between the measurement and simulation result can be seen.

To demonstrate the DDMZM based MPHT has the ability to generate in-phase and quadrature phase RF signals over a wide frequency range using the available equipment, the WDM was replaced by a tunable optical bandpass filter (TOBPF) (Alnair Lab BVF-300CL) that had a sharp edge roll off of 12 dB/GHz. The TOBPF can largely suppress the unwanted first order sideband at frequencies of few GHz away from the optical carrier. The dashed lines in Fig. 12 show the TOBPF magnitude response required to filter out the unwanted lower and upper sidebands at the DDMZM output. The corresponding TOBPF output optical spectrums when the DDMZM is driven by a 15 GHz RF signal and the modulation index is 0.4, are also shown in the figure. Based on the TOBPF magnitude responses shown in Fig. 12, over 40 dB suppression in the unwanted first order sidebands at the frequency of ±6 GHz away from the optical carrier can be obtained. Fig. 13 shows the phase and amplitude responses of the DDMZM based MPHT when using the TOBPF to largely suppress the unwanted sidebands. As shown, the two Hilbert transformer outputs have less than ±1° phase imbalance and less than ±0.3 dB amplitude imbalance in the 6 to 18 GHz frequency range. This demonstrates that the proposed structure can generate in-phase and quadrature phase RF signals with small phase and amplitude imbalance over a wide frequency range.

To demonstrate the DPMZM based MPHT, the DDMZM shown in Fig. 8 was replaced by a DPMZM (Sumitomo T.SBXH1.5-20PD-ADC). A 15 GHz RF signal was applied to the RF port of MZM_A inside the DPMZM. MZM_B RF port was terminated by a 50 Ω terminator. Two DC power supplies were used to provide DC bias voltages to the DPMZM. MZM_A and MZM_B were biased at the null point and the peak point respectively. The DC voltage into the main MZM of the DPMZM was adjusted so that the main MZM bias angle was around 45°. Fig. 14(a) shows the DPMZM output optical spectrum for 0.3 modulation index. An optical carrier and a pair of first order sidebands can be seen. The DPMZM output was connected to the TOBPF. The TOBPF centre wavelength was adjusted to remove the unwanted sidebands. Fig. 14(b) shows the TOBPF magnitude responses and the corresponding optical spectrums at the TOBPF output. The output of the TOBPF was connected to the EDFA, the 0.5 nm 3-dB bandwidth optical filter and the photodetector as in the DDMZM based MPHT. Fig. 15 shows the phase and amplitude responses measured on the VNA connected to the photodetector output. The measurement shows the phase imbalance is within ±1.5° over the 6.3 to 18 GHz frequency range. As shown in Fig. 15(b), the amplitude imbalance is within ±0.35 dB.

The nonlinearity of the two proposed MPHTs was investigated. This was done by applying a 10 GHz RF signal to

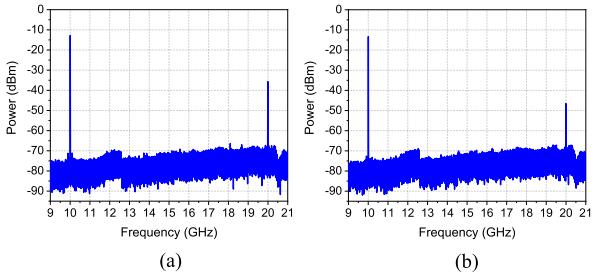

Fig. 16. (a) DDMZM and (b) DPMZM based MPHT output electrical spectrums.

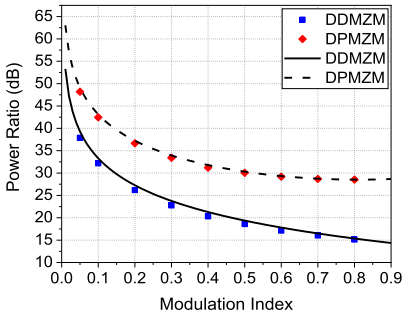

Fig. 17. Measured (dots) and simulated (lines) DDMZM and DPMZM based MPHT fundamental to second order harmonic power ratio versus modulation index.

the DDMZM and DPMZM based MPHTs and measuring the output RF signal power and the second order harmonic power. The WDM with magnitude responses shown in Fig. 9(b) was connected to the modulator output to suppress the unwanted sidebands. The power of the input RF signal and the gain of the EDFA connected to the WDM output were adjusted so that the modulation index was 0.4 and the average optical power into the photodetector was 8 dBm for the two MPHTs. Fig. 16 shows the two MPHT output electrical spectrums. This shows the two MPHTs have almost the same output RF signal power but the fundamental to second order harmonic power ratio of the DDMZM and DPMZM based MPHT is 22.8 dB and 33.2 dB respectively. The results indicate that the DPMZM based MPHT has 10.4 dB improvement in the second order harmonic suppression compared to the DDMZM based MPHT. The fundamental to second order harmonic power ratios of the two MPHTs were measured when the modulation index changed from 0.05 to 0.8. Fig. 17 shows the measurements together with the simulated power ratios obtained using 20 dB unwanted first order sideband suppression, which is close to that found from the WDM magnitude responses. Close agreement between the measured and simulated power ratios can be seen. The second order harmonic generated by the DPMZM based MPHT is around 10 dB less than that generated by the DDMZM structure. Finally, the WDM in the DDMZM and DPMZM based MPHTs was replaced by the TOBPF. Since the TOBPF magnitude response has a sharp edge roll off, the unwanted first order sideband at the frequency of 10 GHz away from the optical carrier is largely suppressed by the TOBPF. Fig. 18 shows the output electrical spectrums of the two proposed MPHTs. As shown in the figure, the fundamental

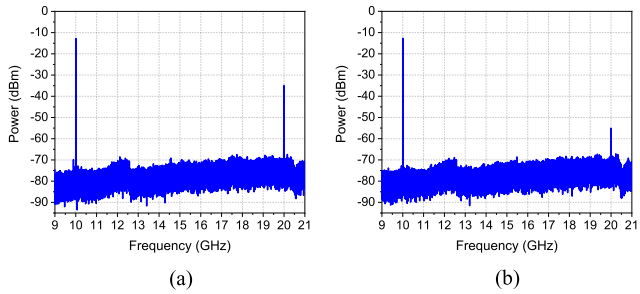

Fig. 18. (a) DDMZM and (b) DPMZM based MPHT output electrical spectrums when the TOBPF is used to filter out the unwanted sidebands.

to second order harmonic power ratio of the DDMZM based MPHT is 22.2 dB, which is almost the same as that when using the WDM for unwanted sideband suppression. On the other hand, the DPMZM based MPHT fundamental to second order harmonic power ratio is 42.4 dB, which is around 10 dB higher than that when using the WDM. This shows, when the unwanted first order sideband is largely suppressed, the DPMZM based MPHT generates very small second order harmonic compared to the DDMZM based MPHT.

V. Conclusion

Two new MPHTs have been presented. They are based on using a DDMZM or a DPMZM for RF signal modulation, and a WDM to separate the lower and upper sideband before photodetection. In-phase and quadrature phase RF signals can be obtained by designing the modulator bias angles. Effects of the residual first order sidebands and the higher order sidebands on the output RF signal phase difference and the Hilbert transformer nonlinearity have been analysed. A commercial modulator bias controller can be incorporated into the DDMZM based MPHT to obtain a long-term stable performance. The phase difference of the two output RF signals generated by the DPMZM based MPHT is independent to the modulation index. Experimental results demonstrate, when the unwanted first order sideband is largely suppressed, the DDMZM based MPHT has less than $\pm 1^\circ$ and ± 0.3 dB phase and amplitude imbalance respectively over the 6 to 18 GHz frequency range. The phase and amplitude imbalance slightly increase to $\pm 1.5^\circ$ and ± 0.35 dB for the DPMZM based MPHT. However, experimental results show the DPMZM based MPHT has a high fundamental to second order harmonic power ratio of 42.4 dB, which is 20 dB higher than that of the DDMZM based MPHT.

References

[1] R. A. Minasian, E. H. W. Chan, and X. Yi, "Microwave photonic signal processing," *Opt. Exp.*, vol. 21, no. 19, pp. 22918–22936, 2013.
[2] R. Zheng, E. H. W. Chan, X. Wang, X. Feng, and B. Guan, "Microwave photonic devices based on liquid crystal on silicon technology," *Appl. Sci.*, vol. 9, no. 2, 2019, Art. no. 260.
[3] A. D. Poularikas, *Transforms and Applications Handbook*. Boca Raton, FL, USA: CRC Press, 2018.
[4] H. Emami, N. Sarkhosh, L. Bui, and A. Mitchell, "Wideband RF photonic in-phase and quadrature-phase generation," *Opt. Lett.*, vol. 33, no. 2, pp. 98–100, 2008.

[5] H. Emami and N. Sarkhosh, "Reconfigurable microwave photonic in-phase and quadrature detector for frequency agile radar," *J. Opt. Soc. Amer. A*, vol. 31, no. 6, pp. 1320–1325, 2014.

[6] Y. Cao, E. H. W. Chan, X. Wang, X. Feng, and B. Guan, "Photonic microwave quadrature filter with low phase imbalance and high signal-to-noise ratio performance," *Opt. Lett.*, vol. 40, no. 20, pp. 4663–4666, 2015.

[7] T. X. H. Huang, X. Yi, and R. A. Minasian, "Microwave photonic quadrature filter based on an all-optical programmable Hilbert transformer," *Opt. Lett.*, vol. 36, no. 22, pp. 4440–4442, 2011.

[8] H. Chen and E. H. W. Chan, "Independent amplitude and phase control of two orthogonal linearly polarised light and its applications," *IEEE Photon. J.*, vol. 13, no. 6, Dec. 2021, Art. no. 7200206.

[9] L. Zhuang, M. R. Khan, W. Beeker, A. Leinse, R. Heideman, and C. Roeloffzen, "Novel microwave photonic fractional Hilbert transformer using a ring resonator-based optical all-pass filter," *Opt. Exp.*, vol. 20, no. 24, pp. 26499–26510, 2012.

[10] M. Tan *et al.*, "Microwave and RF photonic fractional Hilbert transformer based on a 50 GHz Kerr micro-comb," *J. Lightw. Technol.*, vol. 37, no. 24, pp. 6097–6104, Dec. 2019.

[11] Z. Li, Y. Han, H. Chi, X. Zhang, and J. Yao, "A continuously tunable microwave fractional Hilbert transformer based on a nonuniformly spaced photonic microwave delay-line filter," *J. Lightw. Technol.*, vol. 30, no. 12, pp. 1948–1953, Jun. 2012.

[12] H. Shahoei and J. Yao, "Continuously tunable fractional Hilbert transformer by using a single π-phase shifted FBG," *IEEE Photon. Technol. Lett.*, vol. 25, no. 22, pp. 2225–2228, Nov. 2013.

[13] J. Y. Choe, "Defense RF systems: Future needs, requirements, and opportunities for photonics," in *Proc. Int. Topical Meeting Microw. Photon.*, pp. 307–310, 2005.

[14] H. Kiuchi *et al.*, "High extinction ratio Mach-Zehnder modulator applied to a highly stable optical signal generator," *IEEE Trans. Microw. Theory Techn.*, vol. 55, no. 9, pp. 1964–1972, Sep. 2007.

[15] Hybrids, Marki Microwave Inc, 2021. [Online]. Available: https://www.markimicrowave.com/hybrids/hybrids-products.aspx

[16] X. Li *et al.*, "Arbitrary bias point control technique for optical IQ modulator based on dither-correlation detection," *J. Lightw. Technol.*, vol. 36, no. 18, pp. 3824–3836, Sep. 2018.

[17] C. Huang, E. H. W. Chan, and C. B. Albert, "A compact photonics-based single sideband mixer without using high-frequency electrical components," *IEEE Photon. J.*, vol. 11, no. 4, Aug. 2019, Art. no. 7204509.

[18] C. Wang *et al.*, "100-GHz low voltage integrated Lithium Niobate modulators," in *Proc. Conf. Lasers Electro-Opt.*, 2018, pp. 1–2.

[19] Marki Microwave 3 dB quadrature hybrid (QH-0867) datasheet, 2014. [Online]. Available: https://www.markimicrowave.com/Assets/datasheets/QH-0867.pdf

[20] "Microwave power dividers and couplers tutorial," Marki Microwave Application Note, 2021. [Online]. Available: https://www.markimicrowave.com/engineering/application-notes/